

## INVESTIGATION OF CLASSIFIERS FOR EARLY-STAGE BREAST CANCER BASED ON RADAR TARGET SIGNATURES

R. C. Conceição, M. O'Halloran, E. Jones, and M. Glavin <sup>†</sup>

Electrical and Electronic Engineering  
College of Engineering and Informatics  
National University of Ireland Galway  
Ireland

**Abstract**—Ultra Wideband (UWB) radar has been extensively investigated as a means of detecting early-stage breast cancer. The basis for this imaging modality is the dielectric contrast between normal and cancerous breast tissue at microwave frequencies. However, based on the dielectric similarities between a malignant and a benign tumour within the breast, differentiating between these types of tissues in microwave images may be problematic. Therefore, it is important to investigate alternative methods to analyse and classify dielectric scatterers within the breast, taking into account other tumour characteristics such as shape and surface texture of tumours. Benign tumours tend to have smooth surfaces and oval shapes whereas malignant tumours tend to have rough and complex surfaces with spicules or microlobules. Consequently, one classification approach is to classify scatterers based on their Radar Target Signature (RTS), which carries important information about scatterer size and shape. In this paper, Gaussian Random Spheres (GRS) are used to model the shape and size of benign and malignant tumours. Principal Components Analysis (PCA) is used to extract information from the RTS of the tumours, while eight different combinations of tumour classifiers are analysed in terms of performance and are compared in terms of two possible approaches: Linear Discriminant Analysis (LDA) and Quadratic Discriminant Analysis (QDA).

---

Corresponding author: R. C. Conceição (raquelcruzconceicao@gmail.com).

<sup>†</sup> All are also with Bioelectronics Research Cluster, NCBS, National University of Ireland Galway, Ireland.

## 1. INTRODUCTION

Microwave Imaging (MI) has been comprehensively investigated as a means of detecting tumours within the breast, and is based on the dielectric contrast between different types of tissue at microwave frequencies. Three different MI approaches have been investigated by many authors: Microwave Tomography, Time-Reversal FDTD methods and UWB Radar Imaging. In this study only UWB is addressed so for further detail on Microwave Tomography the reader is advised to refer to [1–6] and for Time-Reversal Finite-Difference Time-Domain (FDTD) method to [7–9].

When the breast is illuminated by a UWB pulse, reflections are generated by dielectric scatterers, such as tumours. These reflections can be processed to produce an image of the breast, where high energy regions suggest the possible presence of cancerous tissue. Historical studies such as those by Joines et al. [10] and Surowiec et al. [11] found significant dielectric contrast between normal and cancerous tissue in the breast.

Historically, many studies have examined UWB Radar imaging to detect early stage breast cancer. Hagness et al. [12] developed one of the first UWB beamforming algorithms based on the Confocal Microwave Imaging (CMI) approach. More recently, a series of beamformers have been developed in studies such as [13–20], with different antenna configurations compared in studies such as [21–23]. Finally, in [24, 25] a UWB Radar system to detect breast cancer is described.

However, recent findings by Lazebnik et al. [26, 27] have found that the dielectric contrast between benign and malignant tumour may not be as significant as indicated in previous studies. Therefore, it is important to develop a good imaging modality that allows not only to identify but also to classify tumours, as UWB imaging on its own may not be sufficient.

Chen et al. [28, 29] addressed the issue of tumour classification by analysing the effect that different tumours had on the late-time response of backscattered signals from a 2D FDTD breast model, and more recently, in [30], he included the use of a contrast-agent which is applied to the lesions in order to increase the contrast between tumour tissues and normal breast tissue. In previous work, Davis et al. [31] investigated the RTS of dielectric scatterers within the breast in order to characterise tumours as either benign or malignant. In her paper, Davis created tumour models based on GRS — first introduced by Muinonen [32] — which represent the different stages of growth of a tumour through a range of shapes and sizes.

The tumour classification process is composed of three distinct steps:

- PCA on each backscattered signal.
- Dimensionality reduction.
- Classification using both LDA [31,33–36] and QDA approaches [33–36].

This paper investigates the development of a classifier which distinguishes the different types of tumours (malignant or benign), using shape and size as the key characteristics. There are three significant differences between this study and the previous work of Davis [31]:

- The classifiers used in this study are designed in different architectures that are combinations of coarse and/or fine size and shape classifiers;
- A fourth tumour model is introduced: the macrolobulated GRS which represents a benign tumour in a stage of development that may indicate that a tumour is in a pre-malignant stage. The introduction of this tumour model is significant because it is particularly important to classify tumours at the earliest stage of development possible;
- QDA is investigated as a method for classification.

The remainder of the paper is organized as follows: Section 2 describes the GRS method used to model the growth patterns of benign and malignant tumours; Section 3 introduces both the PCA method applied to the RTS and the LDA and QDA methods; Section 4 describes the breast model (incorporating the GRS tumour models) developed to generate representative UWB backscattered signals; finally, the results and conclusions are presented in Section 5.

## 2. TUMOUR MODELS

Tumours present different characteristics based on their type, i.e., whether they are benign or malignant. The most relevant features from the perspective of UWB imaging are size, shape and texture of surface, as these are characteristics that most significantly influence the RTS of tumours. Benign tumours typically have smooth surfaces and have spherical, oval or at least well-circumscribed contours. Conversely, malignant tumours usually present rough and complex surfaces with spicules or microlobules, and their shapes are typically irregular, ill-defined and asymmetric. Although size may play an important role when analysing the development of a tumour over a period of time and

may be an indication of malignancy, in this study the primary concern is the analysis of small tumours (up to 1 cm in radius), therefore shape and texture of the surface of a tumour are the two most important characteristics that will help differentiate between a benign and a malignant tumour [37–40].

The tumour models are based on the GRS method [31, 32, 41]. GRS can be modified mathematically to model both malignant and benign tumours by varying the mean radius ( $\alpha$ ) and the covariance function of the logarithmic radius (or simply logradius). The shape,  $r = r(\vartheta, \varphi)$ , is described in spherical coordinates  $(r, \vartheta, \varphi)$  by the spherical harmonics series for the logradius  $s = s(\vartheta, \varphi)$ :

$$r(\vartheta, \varphi) = \alpha \exp \left[ s(\vartheta, \varphi) - \frac{1}{2} \beta^2 \right] \quad (1)$$

$$s(\vartheta, \varphi) = \sum_{l=0}^{\infty} \sum_{m=-l}^l s_{lm} Y_{lm}(\vartheta, \varphi). \quad (2)$$

In the equations above,  $\beta$  is the standard deviation of the logradius,  $s_{lm}$  are the spherical harmonics coefficients and  $Y_{lm}$  are the orthonormal spherical harmonics.

Four different models of tumours at four different sizes are considered in this paper. Malignant tumours are represented by spiculated and microlobulated GRS, whereas benign tumours are modeled with macrolobulated and smooth GRS. Microlobulated, macrolobulated and smooth GRS are obtained by varying the correlation angle from low to high. Spiculated GRS are obtained by adding 3, 5 or 10 spicules to smooth GRS. The average radius of all types of spheres are 2.5, 5, 7.5 or 10 mm [31, 32]. Between all sizes and shapes, the number of tumour models developed was 288. A sample of each of the four shapes of the GRS, with a radius of 5 mm, is shown in Figure 1.

### 3. TUMOUR CLASSIFICATION ALGORITHM

The tumour classification is accomplished through an algorithm which analyses the RTS of the tumours. Firstly, PCA is applied to each recorded backscattered signal. This is followed by a dimensionality reduction in which the more representative Principal Components of the data are extracted. Finally, two classification methods are applied to the selection of Principal Components: LDA and QDA. These stages of the classification algorithm are detailed in the following two subsections.

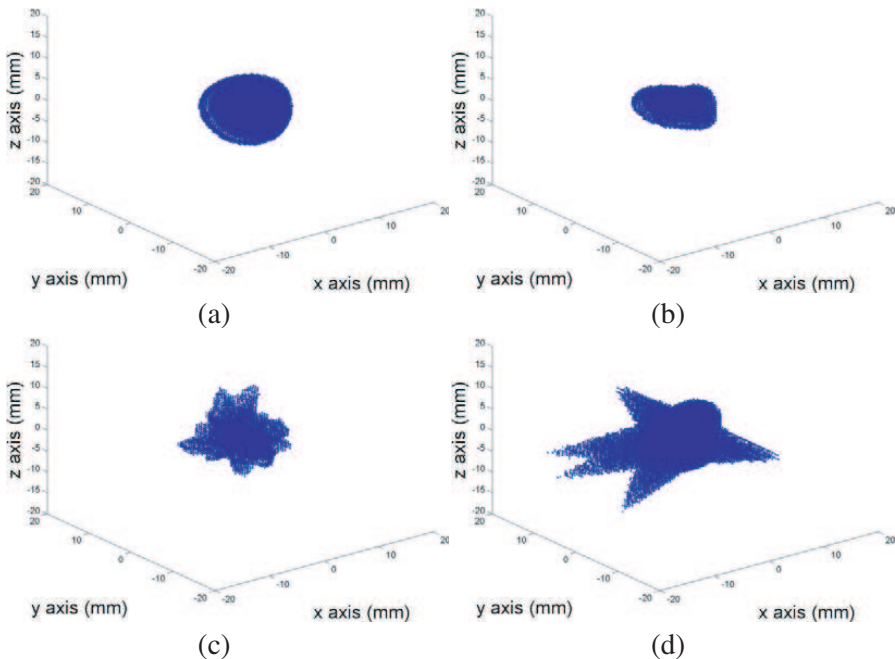


**Figure 1.** Samples of different Gaussian Random Spheres. From left to right, top to bottom: (a) smooth, (b) macrolobulated, (c) microlobulated and (d) spiculated (5 spicules) models, with an average radius size of 5 mm.

### 3.1. Principal Components Analysis

In order to analyse the RTS of the tumours it is important to use a method to extract the most significant bases of the recorded backscattered signals of each tumour so that the classification can be applied more efficiently. The method used in this study is called PCA, which reduces the dimensionality of multivariate data and reveals simplified structures that are often hidden in the original data set while also disregarding less relevant information such as noise or colinearities in signals [42, 43].

This process is accomplished when, by means of a linear algebraic operation, the basis that was used to record the original signals is changed into one new orthonormal basis, or rows of vectors, that allows the best representation to discriminate the original data set, i.e., when the new data set presents maximal variance. The principal components are ordered by decreasing variance, and furthermore the variance along each principal component provides a measurement of the relative importance of each dimension [43].

It must also be noted that PCA is non-parametric, meaning that the data on its own is sufficient to calculate its principal components by means of its sample mean and sample covariance matrix, disregarding how the data was acquired or the need of any type of parameters. However, it must be added that PCA does not explicitly identify the optimal basis for discriminating among the analysed class labels and so the PCA results must be appropriately dimensioned and classified [31, 43]. For the sake of computational simplicity, the original data should be well represented with the minimum number of principal components, thus creating a problem with the least number of dimensions possible [44].

To obtain the principal components of a matrix  $X$  represented by  $(m \times n)$ , where  $m$  is the number of measurements and  $n$  is the number of samples, the mean of the sample for each  $i$ th measurement is subtracted and finally the basis vectors  $\mathbf{h}_m$ , which are the eigenvectors of the covariance matrix  $\mathbf{C} = E\{\hat{\mathbf{X}}\hat{\mathbf{X}}^T\}$ , are calculated. The centered data is represented, for each  $i$ th measurement, by its Karhunen-Loève expansion:

$$\hat{\mathbf{X}} = \mathbf{X} - E\{\mathbf{X}\} = \sum_{m=1}^{N_m} \theta_m \mathbf{h}_m, \quad (3)$$

in which,  $\theta_m$  represents each basis expansion coefficient and  $N_m$  represents the full dimensionality of the problem [31, 43].

### 3.2. Classifiers Based on Linear and Quadratic Discriminant Analysis

Two classification methods are investigated in this paper: LDA [31, 33–36] and QDA [33–36].

LDA is used under the assumption that the groups being discriminated have multivariate normal distributions and have the same covariance matrix. With the LDA method, the pooled within-group covariance matrix is calculated and used to determine the discriminant function which will allow classification [33–36]. QDA is usually applied when the groups being discriminated have significantly different group-specific covariance matrices, while the group populations represent multivariate normal distributions with the same mean [33–35]. Generally, QDA offers increased flexibility over LDA at the cost of possibly ‘overfitting’ the training sample [33].

Both LDA and QDA classifiers are applied to the data using the cross-validation method so that the performance of each classifier is evaluated using a testing set, independent from the training set [45]. The cross-validation method is as follows: to test the whole set of 288 tumours, the set is divided in  $A$  subsets, each of which contains

one sample of each type and each size of tumour; each subset is then tested against the remaining  $(A - 1)$  subsets and, finally, all resulting  $A$  sub-classifications are averaged to obtain the performance of each classifier.

Eight different classifier architectures are considered, five of which first classify the RTS by size and then by shape, and the other three only classify the RTS by shape. The different architectures are defined by the size and shape granularity, i.e., how many categories are classified in each step (two or four categories), and by the number of steps each size and/or shape classifier is composed of (one or two steps). It must be emphasized that a coarse shape classifier is used to classify tumours into either malignant or benign tumours, which may give sufficient information to the patient. However, extra granularity in the shape classifier allows further classification of tumours into spiculated, microlobulated (both malignant tumours) and in macrolobulated and smooth (both benign tumours), giving important clinical information on the development stage of a breast tumour.

The first classifier architecture, Coarse-Shape (CS), splits the RTS in one step into two shape groups: malignant or benign. Similarly, the Fine-Shape (FS) initially classifies the RTS into the same shape categories as the CS, but then adds another level of shape granularity by dividing malignant tumours into spiculated and microlobulated tumours and benign tumours into macrolobulated and smooth tumours.

The Coarse-Size-Coarse-Shape (CSCS) splits the RTS in one step into two size groups (the first group has 2.5 and 5 mm tumours and the second has 7.5 and 10 mm tumours), before further classifying the tumours into either benign or malignant. Similarly, the Coarse-Size-Fine-Shape (CSFS) initially classifies the RTS into the same size and shape categories as the CSCS, but then adds another level of shape granularity by dividing malignant tumours into spiculated and microlobulated tumours and benign tumours into macrolobulated and smooth tumours in a second step of classification.

The Fine-Size-Coarse-Shape (FSCS) and Fine-Size-Fine-Shape further classify the RTS into four subcategories of size (2.5 mm, 5 mm, 7.5 mm and 10 mm) in two steps. The FSCS then divides them into two categories of tumour, benign and malignant, while the FSFS classifies them into four shape categories: spiculated, microlobulated, macrolobulated and smooth in two steps.

The Direct-Fine-Shape (DFS) performs the same function as the FS classifier, but divides the RTS into four shape categories in one step. The Direct-Fine-Size-Fine-Shape (DFSFS) performs the same function as the FSFS classifier, but divides the RTS into four size categories in

one step, and similarly classifies the RTS into the four shape categories in a single step.

#### 4. MODEL OF THE BREAST

A 3D FDTD model of the breast was developed which incorporates the dielectric properties within the breast. A half millimeter resolution cubic grid was used for the FDTD model. In order to analyse the RTS of the tumours, the backscattered data was generated by means of a Total-Field/Scattered-Field (TF/SF) simulation [31, 46], as previously used by Davis et al. [31].

The Scattered Field (SF) is a square geometric prism with the square bases measuring 153.5 mm and the height measuring 137.5 mm. The Total Field (TF) is represented by a 50 mm cube and is located at the centre of the SF, and the origin of the system (0, 0, 0) mm corresponds to the centre of the TF. The TF/SF region is terminated with a 6 mm-layer Uniaxial Perfectly Matched Layer (UPML) which suppresses any boundary reflections [31, 47].

The tumour is modeled with the Debye parameters for malignant tissue whereas the normal breast tissue and the surrounding media is modeled with the Debye parameters for homogeneous lossy adipose tissue, as established by Lazebnik et al. [26, 27]. The Debye parameters for malignant tissue are as follows:  $\epsilon_\infty = 6.749$ ,  $\Delta\epsilon = 50.09$  and  $\sigma_s = 0.794 \text{ Sm}^{-1}$ . The Debye parameters for homogeneous lossy adipose tissue are as follows:  $\epsilon_\infty = 3.140$ ,  $\Delta\epsilon = 1.592$  and  $\sigma_s = 0.036 \text{ Sm}^{-1}$ .

A pulsed plane wave is transmitted towards the target from four different equidistant angles (0, 90, 180 and 270°) and the resulting cross-polarized backscatter is recorded and analysed from four observation points located at: (0, 0, -74), (-74, 0, 0), (0, 0, 74) and (74, 0, 0) mm, in ( $x, y, z$ ) axes. The incident pulse was a modulated Gaussian pulse with center frequency at 6 GHz where the  $1/e$  full temporal width of the Gaussian envelop was 160 ps [31]. The pulse is linearly polarized in the  $y$  and  $x$  direction and transmitted in the  $z$  direction. Each observation point is located in the Scattered Field at a distance of 74 mm from the center of the tumour, which is located at the center of the Total Field. The acquired backscattered recorded signals are then downsampled from 1200 GHz to 75 GHz.

Figure 2 shows a representation of the TF/SF grid, with the location of the origin of the first incident plane wave and respective observer point (▲) as well as the position of the tumour.

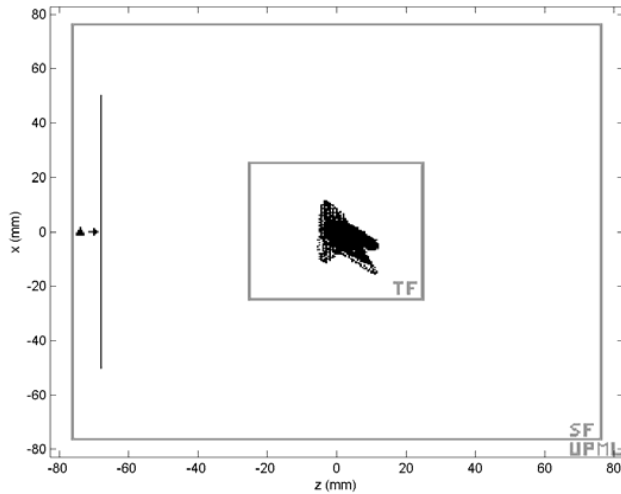


**Figure 2.** Cross-section of the 3D FDTD space lattice partitioned into Total Field (TF), Scattered Field (SF) and UPML regions. The target, a spiculated tumour located at the centre of the TF, is illuminated by a pulsed plane wave propagating in the  $+z$  direction and backscatter is recorded at the observer location:  $(0, 0, -74)$  mm (represented by  $\blacktriangle$ ).

## 5. RESULTS AND DISCUSSION

For all results, a database of 288 models was used for testing and training the classifiers, using the cross-validation method described in Section 3.2. For both size and shape classifiers the performance of the classifications was observed against the number of PCA components (data not shown) and results indicated that 30 principal components are suitable as the classification performance starts to saturate at this level. The use of 30 principal components offers a good compromise between classification accuracy and computational time, which had also been found in [31].

There are two subsections in this section: the first subsection analyses the performance of the eight possible architectures for the classifiers and the second subsection compares the LDA and the QDA approaches.

### 5.1. Analysis of the Performance of the Eight Classification Architectures

The results for the eight different architecture of classifiers are presented in Table 1, which presents the groups in which models are

classified and the corresponding accuracy results. The accuracy results are shown in three columns:

- the first column presents the partial accuracy for the size classification
- the second column presents the partial accuracy for the shape classification
- the third column presents the overall accuracy for each cascade classifier that follow the size-then-shape structure.

The accuracy of the partial size or the partial shape classifier is expressed in terms of the proportion of tumours correctly identified in terms of size or shape, respectively, in isolation. The overall accuracy for the size-then-shape cascade classifier is calculated by multiplying the partial accuracies for the size and shape classifiers and represents the percentage of tumours correctly classified in terms of both size and then shape.

**Table 1.** Accuracy for size and subsequent shape classifiers and overall size-then-shape cascade classifier using both LDA and QDA classifications for eight different architectures of classifiers.

<i>Architectures of classifiers</i>	<i>Partial size classifier (%)</i>	<i>Partial shape classifier (%)</i>	<i>Size-then-shape classifier (%)</i>
Coarse-Shape	N/A	80.90 (LDA) 84.03 (QDA)	N/A
Fine-Shape	N/A	58.33 (LDA) 55.90 (QDA)	N/A
Coarse-Size- Coarse-Shape	93.05 (LDA) 91.32 (QDA)	87.15 (LDA) 82.29 (QDA)	81.10 (LDA) 75.13 (QDA)
Coarse-Size- Fine-Shape	93.05 (LDA) 91.32 (QDA)	67.36 (LDA) 62.15 (QDA)	62.68 (LDA) 56.76 (QDA)
Fine-Size- Coarse-Shape	79.86 (LDA) 72.22 (QDA)	86.80 (LDA) 84.72 (QDA)	69.32 (LDA) 61.19 (QDA)
Fine-Size- Fine-Shape	79.86 (LDA) 72.22 (QDA)	69.44 (LDA) 64.58 (QDA)	55.46 (LDA) 46.64 (QDA)
Direct-Fine- Shape	N/A	59.03 (LDA) 52.08 (QDA)	N/A
Direct-Fine-Size- Fine-Shape	76.39 (LDA) 72.22 (QDA)	62.50 (LDA) 63.89 (QDA)	47.74 (LDA) 46.14 (QDA)

Before examining the results from Table 1 in detail, the manner in which errors propagate when a partial coarse size (or shape) classifier is extended to a fine classifier must be considered. The implication of the fine-size (or fine-shape) architecture is that any misclassified tumours in the first step of the size (or shape) classification — which also corresponds to the results of the coarse classifier — are necessarily misclassified in the second step of size (or shape) classification, and therefore an error propagation takes place. An example in which this error propagation is most noticeable is for the first two classifier architectures: CS to FS, where the increase of granularity of the shape classification results in a decrease in the accuracy of 22.57% (LDA) and 28.13% (QDA).

Examining the CS/FS, CSCS/CSFS and FSCS/FSFS architectures in Table 1 shows that the accuracy for the partial shape classification is considerably higher when a previous size classifier is used, in particular a fine size classifier (FSCS/FSFS architectures), for both LDA and QDA — with an exception for the shape classifier in CSCS when using QDA as the correspondent performance in CS is higher by 1.74%. Even though the accuracy of the fine size classifier is lower than the coarse classifier, the fact that the fine size classifier has higher granularity allows for better accuracy results in the following shape classifier.

Finally, examining the overall performance of the classifiers, there are several significant findings:

- When considering the overall accuracy of the size-then-shape cascade classifier, the accuracy of the cascade classifiers tends to worsen with increasing number of steps in the partial size and/or shape classifications, i.e., when fine-size and/or fine-shape classifiers are used. The accuracy drops by 25.44% (LDA) and by 37.39% (QDA) from a coarse classifier with one step (CS) to a fine classifier with four steps (FSFS).
- FS and DFS are the least accurate shape classifiers, leading to the conclusion that a shape classifier is more accurate when preceded by a size classifier.
- There was very little performance difference between the FSFS and DFSFS classifiers, the overall size-then-shape cascade classifier accuracy of FSFS was 55.46% (LDA) and 46.64% (QDA) whereas for DFSFS it was 46.64% (LDA) and 46.14% (QDA).
- The best classifier to simply detect whether a tumour is malignant or benign is FSCS with QDA and CSFS with LDA, in which a fine-size and a coarse-size classifiers are used respectively. In terms of highest granularity in both size and shape, FSFS and DFSFS

performed better with LDA instead of QDA. However it must also be noted that DFSFS results do not deteriorate to the same extent as FSFS when using the alternative discriminant analysis method.

- To obtain a clearer discrimination of the shape of tumours beyond simply malignant and benign (spiculated, microlobulated, macrolobulated or smooth), the FSFS, which involves a fine-size and fine-shape classifier, performs best.

## 5.2. Comparison of the LDA and the QDA Approaches

Overall, LDA and QDA output similar results for the same architectures or, at least, they tend to output results that reflect the same trends when comparing the different architectures.

Next, LDA and QDA are examined in the context of the best architectures established in Section 5.1. The best classifier to simply differentiate between a malignant and benign tumour is FSCS, which works better when the LDA method is used, achieving a partial shape accuracy of 86.80% (compared to 84.72% achieved with QDA). In terms of the accuracy of the size-then-shape cascade classifier for the FSCS, the LDA method once again offers improved performance: 69.32% (as opposed to 61.19% with the QDA approach).

The architectures that provide higher granularity in terms of shape are FSFS and DFSFS. FSFS has higher performance when the LDA approach is used, as shown by the partial shape classifier which has an accuracy of 69.44% (compared to 64.58% achieved with QDA). On the other hand, DFSFS has higher performance when the QDA approach is used, as shown by the partial shape classifier which has an accuracy of 63.89% (compared to 62.50% achieved with LDA). Similar conclusions are drawn when analysing the accuracy of the size-then-shape cascade classifier. FSFS promises higher performance with the LDA approach: 55.46% (as opposed to 46.64% through QDA); similarly DFSFS promises higher performance with the LDA approach: 47.74% (as opposed to 46.14% possible through QDA).

## 6. CONCLUSIONS AND FUTURE WORK

In this paper, a number of different methods for diagnosing the type (malignant or benign), and ultimately diagnosing the stage of development (spiculated, microlobulated, macrolobulated and smooth) of breast tumours, are analysed. The type of tumours was correctly classified with an accuracy of 86.80% when the LDA was applied to a FSCS architecture, under these experiment conditions. In terms of the stage of development of the tumours, the models were correctly

classified with an accuracy of 63.89% when the QDA was applied to a DFSFS architecture, and the highest accuracy obtained was of 69.44% when the LDA was applied to a FSFS architecture, under these experiment conditions. Overall, these results are very promising for improved diagnosis and treatment of early-stage breast cancer within the context of UWB Radar Imaging.

Future work will include the investigation of alternative classification algorithms including Support Vector Machines (SVM) and Spiking Neural Networks. The effects of dielectric heterogeneity will also be addressed in future work.

## ACKNOWLEDGMENT

This work is supported by Science Foundation Ireland (SFI) under grant number 07/RFP/ENEF420.

## REFERENCES

1. Meaney, P. M., et al., "Nonactive antenna compensation for fixed-array microwave imaging: Part II — Imaging results," *IEEE Transactions on Medical Imaging*, Vol. 18, No. 6, 508–518, 1999.
2. Meaney, P. M., et al., "A clinical prototype for active microwave imaging of the breast," *IEEE Transactions on Microwave Theory and Techniques*, Vol. 48, No. 11, 1841–1853, 2000.
3. Meaney, P. M., et al., "Initial clinical experience with microwave breast imaging in women with normal mammography," *Academic Radiology*, Vol. 14, No. 2, 207–218, 2007.
4. Bulyshev, A. E., et al., "Computational modeling of three-dimensional microwave tomography of breast cancer," *IEEE Transactions on Biomedical Engineering*, Vol. 48, No. 9, 1053–1056, 2001.
5. Souvorov, A. E., et al., "Two-dimensional computer analysis of a microwave flat antenna array for breast cancer tomography," *IEEE Transactions on Microwave Theory and Techniques*, Vol. 48, No. 8, 1413–1415, 2000.
6. Liu, Q. H., et al., "Active microwave imaging I — 2-D forward and inverse scattering methods," *IEEE Transactions on Microwave Theory and Techniques*, Vol. 50, No. 1, 123–133, 2002.
7. Kosmas, P. and C. M. Rappaport, "Time reversal with the FDTD method for microwave breast cancer detection," *IEEE Transactions on Microwave Theory and Techniques*, Vol. 53, No. 7, 2317–2323, 2005.

8. Kosmas, P. and C. M. Rappaport, "FDTD-based time reversal for microwave breast cancer detection — Localization in three dimensions," *IEEE Transactions on Microwave Theory and Techniques*, Vol. 54, No. 4, 1921–1927, 2006.
9. Kosmas, P. and C. M. Rappaport, "A matched-filter FDTD-based time reversal approach for microwave breast cancer detection," *IEEE Transactions on Antennas and Propagation*, Vol. 54, No. 4, 1257–1264, 2006.
10. Joines, W. T., et al., "The measured electrical properties of normal and malignant human tissues from 50 to 900 MHz," *Medical Physics*, Vol. 21, No. 4, 1994.
11. Surowiec, A. J., et al., "Dielectric properties of breast carcinoma and the surrounding tissues," *IEEE Transactions on Biomedical Engineering*, Vol. 35, No. 4, 257–263, 1988.
12. Hagness, S. C., A. Taflove, and J. E. Bridges, "Two dimensional FDTD analysis of a pulsed microwave confocal system for breast cancer detection: Fixed-focus and antenna-array sensors," *IEEE Transactions on Biomedical Engineering*, Vol. 45, 1470–1479, 1998.
13. O'Halloran, M., M. Glavin, and E. Jones, "Channel-ranked beamformer for the early detection of breast cancer," *Progress In Electromagnetics Research*, Vol. 103, 153–168, 2010.
14. O'Halloran, M., R. C. Conceicao, D. Byrne, M. Glavin, and E. Jones, "FDTD modeling of the breast: A review," *Progress In Electromagnetics Research B*, Vol. 18, 1–24, 2009.
15. Li, X. and S. C. Hagness, "A confocal microwave imaging algorithm for breast cancer detection," *IEEE Microwave and Wireless Components Letters*, Vol. 11, No. 3, 130–132, 2001.
16. Li, X., et al., "An overview of ultra-wideband microwave imaging via space-time beamforming for early-stage breast-cancer detection," *IEEE Antennas and Propagation Magazine*, Vol. 47, No. 1, 19–34, 2005.
17. Bond, E. J., et al., "Microwave imaging via space-time beamforming for early detection of breast cancer," *IEEE Transactions on Antennas and Propagation*, Vol. 51, No. 8, 1690–1705, 2003.
18. O'Halloran, M., M. Glavin, and E. Jones, "Quasi-multistatic MIST beamforming for the early detection of breast cancer," *IEEE Transactions on Biomedical Engineering*, Vol. 57, No. 4, 830–840, 2009.
19. Lim, H. B., et al., "Confocal microwave imaging for breast

- cancer detection: Delay-multiply-and-sum image reconstruction algorithm,” *IEEE Transactions on Biomedical Engineering*, Vol. 55, No. 6, 1697–1704, 2008.
20. O’Halloran, M., M. Glavin, and E. Jones, “Effects of fibroglandular tissue distribution on data-independent beamforming algorithms,” *Progress In Electromagnetics Research*, Vol. 97, 141–158, 2009.
  21. Conceicao, R. C., M. O’Halloran, M. Glavin, and E. Jones, “Comparison of planar and circular antenna configurations for breast cancer detection using microwave imaging,” *Progress In Electromagnetics Research*, Vol. 99, 1–19, 2009.
  22. Fear, E. C., et al., “Confocal microwave imaging for breast cancer detection: Localization of tumors in three dimensions,” *IEEE Transactions on Biomedical Engineering*, Vol. 49, No. 8, 812–822, 2002.
  23. Conceicao, R. C., M. O’Halloran, M. Glavin, and E. Jones, “Antenna configurations for Ultra Wide Band radar detection of breast cancer,” *Proceedings of the SPIE*, Vol. 7169, San Jose, California, 2009.
  24. Klemm, M., et al., “Breast cancer detection using symmetrical antenna array,” *Antennas and Propagation, 2007. EuCAP 2007. The Second European Conference*, Edinburgh, UK, 2007.
  25. Craddock, I. J., et al., “Development and application of a UWB radar system for breast imaging,” *2008 Loughborough Antennas & Propagation Conference*, 2008.
  26. Lazebnik, M., et al., “A large-scale study of the ultrawideband microwave dielectric properties of normal breast tissue obtained from reduction surgeries,” *Physics in Medicine and Biology*, Vol. 52, 2637–2656, 2007.
  27. Lazebnik, M., et al., “A large-scale study of the ultrawideband microwave dielectric properties of normal, benign and malignant breast tissues obtained from cancer surgeries,” *Physics in Medicine and Biology*, Vol. 52, 6093–6115, 2007.
  28. Chen, Y., et al., “Effect of lesion morphology on microwave signature in ultra-wideband breast imaging: A preliminary two-dimensional investigation,” *2007 IEEE Antennas and Propagation Society International Symposium*, 2007.
  29. Chen, Y., et al., “Effect of lesion morphology on microwave signature in 2-D ultra-wideband breast imaging,” *IEEE Transactions on Biomedical Engineering*, Vol. 55, No. 8, 2011–2021, 2008.
  30. Chen, Y., I. J. Craddock, and P. Kosmas, “Feasibility study

- of lesion classification via contrast-agent-aided UWB breast imaging,” *IEEE Transactions on Biomedical Engineering*, Vol. 57, No. 5, 1003–1007, 2010.
31. Davis, S. K., et al., “Breast tumor characterization based on ultrawideband microwave backscatter,” *IEEE Transactions on Biomedical Engineering*, Vol. 55, No. 1, 237–246, 2008.
  32. Muinonen, K., “Introducing the Gaussian shape hypothesis for Asteroids and Comets,” *Astronomy and Astrophysics*, Vol. 332, 1087–1098, 1998.
  33. Everitt, B. S. and G. Dunn, *Applied Multivariate Data Analysis*, 2nd edition, Arnold Publishers, New York, 2001.
  34. Seber, G. A. F., *Multivariate Observations*, John Wiley & Sons, Inc, Hoboken, New Jersey, 1984.
  35. Krzanowski, W. J., *Principles of Multivariate Analysis: A User’s Perspective*, Oxford University Press, New York, 1988.
  36. Raykov, T. and G. A. Marcoulides, “An introduction to applied multivariate analysis,” Routledge Taylor & Francis Group, New York, 2008.
  37. Conceicao, R. C., et al., “Classification of suspicious regions within ultrawideband radar images of the breast,” *16th IET Irish Signals and Systems Conference, ISSC 2008*, Instn. Engg. & Tech., Galway, Ireland, UK, 2008.
  38. Rangayyan, R. M., et al., “Measures of acutance and shape for classification of breast tumors,” *IEEE Transactions on Medical Imaging*, Vol. 16, No. 6, 799–810, 1997.
  39. Guliato, D., et al., “Polygonal modeling of contours of breast tumors with the preservation of spicules,” *IEEE Transactions on Biomedical Engineering*, Vol. 55, No. 1, 14–20, 2008.
  40. Nguyen, T. M. and R. M. Rangayyan, “Shape analysis of breast masses in mammograms via the fractal dimension,” *Engineering in Medicine and Biology 27th Annual Conference*, IEEE, Shangai, China, 2005.
  41. Muinonen, K., “Chapter 11: Light scattering by stochastically shaped particles,” *Light Scattering by Nonspherical Particles: Theory, Measurements, and Applications*, M. I. Mishchenko, J. W. Hovenier, and L. D. Travis, Editors, Academic Press, 2000.
  42. Wold, H., “Estimation of principal components and related models by iterative least squares,” *Multivariate Analysis*, K. R. Krishnaiah, Editor, 391–420, Academic Press, New York, 1996.
  43. Shlens, J., “A tutorial on principal component analysis,”

- Mar. 25, 2003. Available: <http://www.cs.princeton.edu/picasso/mats/PCA-Tutorial-Intuition.jp.pdf>.
44. Bartholomew, D. J., et al., "The analysis and interpretation of multivariate data for social scientists," *Texts in Statistical Science*, Chapman & Hall/CRC, USA, 2002.
  45. Hsu, C.-W., C.-C. Chang, and C.-J. Lin, "A practical guide to support vector classification," Apr. 3, 2010. Available: [www.csie.ntu.edu.tw/~cjlin/papers/guide/guide.pdf](http://www.csie.ntu.edu.tw/~cjlin/papers/guide/guide.pdf).
  46. Sullivan, D. M., *Electromagnetic Simulation Using the FDTD Method*, 1st Edition, *IEEE Press Series on RF and Microwave Technology*, R. D. Pollard and R. Booton, Editors, Wiley-IEEE Press, New York, 2000.
  47. Taflove, A. and S. C. Hagness, *Computational Electrodynamics: The Finite-difference Time-domain Method*, 2nd edition, Artech House, Boston, 2000.